Hindawi
Adsorption Science & Technology
Volume 2022, Article ID 8335566, 14 pages
https://doi.org/10.1155/2022/8335566

Research Article

Evaluation of Amine Functionalized Thermal Power Plant Solid Waste for Industrial Wastewater Remediation

Ali Y. Kozbek[1], **Kubilay Şahin**[1], **Ertuğrul Sarı**[1], **Esra Bedir**[1], **Fatma G. Yüce**[1], **Senem Çitoğlu**[1,2] and **Hatice Duran**[1,3]

[1]*Department of Materials Science and Nanotechnology Engineering, TOBB University of Economics and Technology, Ankara 06510, Turkey*
[2]*Acibadem Mehmet Ali Aydınlar University, Biomaterials Center, Ataşehir, İstanbul 34684, Turkey*
[3]*Life Support Center, Hacettepe University Faculty of Medicine, 06230 Ankara, Turkey*

Correspondence should be addressed to Hatice Duran; hduran@etu.edu.tr

Received 27 August 2021; Revised 7 November 2021; Accepted 20 December 2021; Published 17 January 2022

Academic Editor: Selvaraju Narayanasamy

Micro/nanoparticles generated after the combustion of coal/lignite in the thermal power plants were modified with amino groups of (3-aminopropyl) triethoxysilane (APTES). These silane-based functional particles were applied in textile dye (xylenol orange, XO and methyl orange, MO) removal process to deal with an industrial wastewater problem. The maximum adsorption efficiencies of APTES coated micro/nanoparticles for MO and XO dye molecules were calculated to be around 98% and 75%, respectively. The adsorption behavior of the LCFA against dyes is also assessed by investigating the effect of adsorbent dosage, contact time, pH, and temperature. The optimum dye removal was observed at a pH of 4.0, and the equilibrium was achieved within 5 min. The maximum uptake capacities of LCFA-APTES for MO and XO dye molecules were calculated to be around 17.91 and 14.72 mg g^{-1}, respectively. This value is approximately 3 – 5 times higher than the similar adsorbent in the literature. The uptake mechanism of MO and XO dyes onto LCFA-APTES is governed by electrostatic interaction and hydrogen bonding between dye molecules and APTES. The surface chemical modifications and the nature of functional groups were ascertained by scanning electron microscopy (SEM), thermogravimetric analysis (TGA), X-ray fluorescence (XRF), and X-ray photoelectron spectroscopy (XPS). The application of recovered micro/nanoparticles from solid wastes and their utilization for wastewater treatment is important not only for economy of developing countries but also for protecting the environment.

1. Introduction

Fly ash is a byproduct generated by coal/lignite-based thermal power generation has been the backbone of power combustion. It is mainly generated in coal burned power supplier plants and composed of several micro- and nanoscale ingredients. By virtue of those components, fly ash establishes a lot of concerns about the environment, economy, safety, and public health [1]. Although the residual ashes compose of many beneficial components, up to now, these wastes have not been used effectively in areas other than the construction sector. In 2016, around 1.143 billion tons of fly ash were produced worldwide [2], and this number is increasing exponentially every decade. The recycling of fly ash is around 68-70% worldwide [2]. More than 13 million tons of fly ash are produced every year in Turkey [3] with a utilization rate of only 16.7% of which is used mainly in construction sector. Similarly, approximately 25 million tons of fly ash residues have been turned to beneficial applications in the United States [4] mostly in the concrete and cement industry. Fly ash residues were mostly utilized to improve the quality of concrete and to reduce carbon footprint. Nowadays, fly ash started to be used as a cost-effective adsorbent due to its adsorptive features for the removal of various pollutants (i.e., chlorine, mercury) and organic compounds that are hazardous for the environment [5–8].

Textile wastewater effluent is another industrial byproduct which has a negative influence on environmental health. They are discharged in large volumes into the river and streams. Synthetic dyes from textile industry effluent are the main

contaminants. These dyes can be toxic, carcinogenic, and allergenic as well as mutagenic and highly resistant to biodegradation [9]. When these dyes discharge to water resources, they damage to biological diversity and ecosystem. Therefore, the pollution of water resources by textile dyes has been crucial environmental issue. Textile dyes are distinctively categorized such as acidic, basic, reactive, vat, direct, and disperse dyes. Xylenol orange (XO) and methyl orange (MO), the studied dyes, are belong to acidic dyes are often used in textile industry and can adversely affect aquatic environment because it can prevent the sunlight dispersion [10] Because of these facts, some hazardous dyes are on account of the aquatic life by reducing the light infiltration and exceeding the limit values of chemical oxygen demand (COD) [11, 12].

Various techniques have been investigated to remove these hazardous substances including coagulation, flocculation, chemical oxidation, decolorization, ozonation, membrane filtration, and adsorption [12–17]. Among these techniques, owing to its simplicity, efficiency, and economic viability, adsorption is advised as the most prevalent and proficient method for removing dye from water [18]. Extensive variety of adsorbents has been investigated to treat dye-based effluents. Activated carbon, silica (SiO_2), alumina (Al_2O_3), magnetic nanoparticles (such as Fe_3O_4), graphene, and carbon nanotubes (CNTs) are most extensively employed synthetic examples as adsorbents [19–24]. Also, several adsorbents based on ashes including bottom ash, coal fly ash, rice husk ash, bagasse ash, and tobacco stem ash as well as volcanic ash have also been studied for the adsorption of dyes [25–29]. Furthermore, modification of fly ash assists to strengthen the potential of fly ash as a promising adsorbent for even drinking water treatment [30–32]. Surface modification results in adding new active adsorption sites specific to adsorbate of interest.

Nowadays, many research groups focus solely on the improvement of adsorption capacity. In fact, many new adsorbents have been developed and reported with a dye removal efficiency higher than 80%. However, design of low-cost adsorbents, a very short adsorption time that can operate in more environmentally friendly conditions (for example, at neutral pHs) and long-term regeneration ability is also needed for real field application. One of the main motivations of this study is to demonstrate the reuse of a byproduct of thermal power plant as an inexpensive source of nanoparticles. We have tried to show how these particles can be useful absorbents with a simple one-step surface modification, taking advantage of the high surface area.

Recently, the surface functionalization of mesoporous silica has been explored for water remediation application due to specific interaction between surface amino groups with anionic dye molecules [33]. Various physical and covalent approaches were utilized to succeed amine-functionalized mesoporous silica (MS) [34–37]. Nayab et al. [33] have reported that branched polymer brush-based polyethyleneimine functionalized mesoporous silica reached a very high absorption efficiency ($q_{max} = 186.92 \pm 2.78\ mg\ g^{-1}$) toward the anionic dyes. These results highlight the relevance of the developed surface modified nanostructured adsorbents for environmental remediation by proving the high removal efficiency, short adsorption time, and reusability performances.

Herein, we report a facile and economical one-pot surface modification of the lignite coal fly ash (LCFA) for removal of anionic dyes from industrial wastewater. In previous studies, agricultural biomass-based fly ash was also used as organic dye removal [7]. However, biomass ash residues were consisting of irregular-shaped flake-like structure with large pore sizes (from 20 to 500 nm) and pore distributions. Besides, SiO_2 was the major component of ash while herein the composition of LCFA is based on varying amounts of oxides of aluminum, iron, magnesium, and silica nanoparticles. LCFA nanoparticles were functionalized with an amine group, APTES (3-aminopropyltriethyoxysilane) by silanization process. APTES was chosen due to (i) ease of hydrolysis in many solvents (water, ethanol etc.), (ii) ease of self-assembly on oxide surfaces, (iii) high chemical stability upon chemisorption, and most importantly, (iv) residual NH_2 groups that are available as reactive sites for adsorption (i.e., attachment of dyes, biomolecules). Adsorption behavior of LCFA-APTES evaluated against two different anionic dyes (xylenol orange (XO) and methyl orange (MO)) and compared with pristine LCFA. The effects of process parameters such as adsorbent dosage, contact time, solution pH, temperature, and dye concentration were studied in detail to find the maximum uptake capacity of each adsorbent. The mechanism of the adsorption process was predicted by employing the nonlinear Langmuir, the Freundlich isotherm, and modified Langmuir-Freundlich (MLF) models. In addition, the thermodynamics and kinetic parameters affiliated with the adsorption process were also investigated.

2. Materials and Methods

2.1. Materials. LCFA was obtained from a Turkish thermal power plant that is possessive about sharing its name. Nevertheless, LCFA obtained from this company contains approximately 53.19% SiO_2, 27.86% Al_2O_3, 7.02% Fe_2O_3, and 11.93% the other oxides. Phosphoric acid (H_3PO_4, >85%), 3-aminopropyltriethoxysilane (APTES, 98%), sodium hydroxide (>98%), hydrochloric acid (>37%), toluene (99%), and xylenol orange tetrasodium salt (XO) were purchased from Sigma-Aldrich, Germany. Methyl orange and ethanol (>99%) were purchased from Merck, Germany. Also, molecular sieves, 3 Å (beads, 4-8 mesh), was obtained from Sigma-Aldrich to dry toluene, and Whatman filter paper was used for filtering processes.

2.2. Activation of LCFA. LCFA (100 g) was dried at 110°C in an oven overnight to release moisture. Then, LCFA was washed with distilled water three times at 50°C with 400 rpm to remove water soluble impurities. After each washing operation, the mixture is filtered by the Whatman filter paper (12-25 μm). Afterwards, the washed LCFA was dried at 120°C in a vacuum for 3 hours. The activation of LCFA was achieved by immersing in phosphoric acid (H_3PO_4, >85%), stirring (50°C, 600 rpm) for 1h, and then washing with distilled water several times until neutralize the supernatant. Finally, the slurry was centrifuged

(20 min, 6000 rpm) and oven-dried at 100°C in a vacuum for 40 min. The activated LCFA was then subjected to further surface characterization analysis.

2.3. Amine Functionalization of LCFA. After the activation process, APTES functionalized lignite coal fly ash (LCFA-APTES) was prepared according to literature [33]. LCFA (1.0 g) was refluxed at room temperature for 16 hours in dry toluene (100 mL) containing 0.04 mol (9.36 mL) of APTES. The product was filtered, washed with toluene by centrifugation for 20 min at 4000 rpm, and oven-dried at 110°C in vacuum for 18 h.

2.4. Chemical and Morphological Analysis. Scanning electron microscopy (SEM) images and energy dispersive X-ray analysis (EDAX) spectroscopy results were obtained using a Zeiss Evo 50 scanning electron microscope equipped with Oxford EDAX detector. The thermal properties of the LCFAs were analyzed by thermogravimetry using a Q500 V20.13 Build 39 TGA analyzer in N_2 atmosphere at a heating rate of 10°C/min from room temperature to 900°C, and changes in mass were recorded for determination of the organic matter content. The BET-specific surface area of pristine LCFA, activated LCFA, and APTES coated LCFA (LCFA-APTES) was analyzed by an Autosorb iQ Automated Gas Sorption Analyser (Quantachrome Instruments) by measuring N_2 isotherms at 77 K. Before the measurement, the samples were outgassed under an applied temperature (40°C for LCFA-APTES, 150°C for pristine LCFA and activated LCFA) and under vacuum for 19 h. Dry and degassed samples were then subjected to BET for surface area assessment. Cumulative surface area of the pores and mesopore diameter was determined from BJH analysis of the adsorption data. The micropore volume was deduced from *t*-plot analysis (de Boer method). XRF (Rigaku model ZSX Primus II XRF) was used to determine the elemental composition of the LCFA during surface modification steps. X-ray photoelectron spectroscopy (XPS) for elemental compositions and chemical bonding study was performed using Thermo Scientific K-Alpha. The Mg Kα (1486.6 eV) X-ray source was operated at 300 W. The survey scans were carried out with pass energy of 117.40 eV. The spectra were recorded using a 60° take-off angle relative to the LCFA located substrate normal. The UV/vis absorption spectra of the dyes were analyzed using a Hitachi U-5100 spectrophotometer. The zeta potential of the LCFAs was measured at 25°C with a Malvern ZetaNano ZS using a helium–neon laser source of 5 mW at a 633 nm wavelength. The LCFA suspensions were prepared at a concentration of 10 mg mL^{-1} in deionized water. The solution pH range varied between 2 and 12 using 0.1 M HCl and 0.1 M NaOH. The suspension was not sonicated.

2.5. Adsorption and Desorption Studies. The dye uptake capacities of activated LCFA and LCFA-APTES were investigated by using various quantities of adsorbents. Specimens (5 – 25 mg) of both units were stirred at room temperature (350 rpm) with 10 mL aqueous dye solutions of known initial concentration (15 ppm for both dyes) at optimized contact time (t) and pH. Optimization of contact time, temperature, and pH was obtained by series of analyzes. pH = 4, t = 5 min, and T = 25°C are defined as the optimum parameters for each dye. At the end of the adsorption process, the filtrate was centrifuged (7 min, 6000 rpm), and the concentration of each dye in the supernatant liquid before and after the adsorption was obtained by using a calibration curve investigated by employing a UV/vis spectrophotometer at λ_{max} of 436 nm for XO and λ_{max} of 470 nm for MO.

The amount of dye adsorbed at equilibrium q_e (mg g^{-1}) can be calculated by Equation (1):

$$q_e = \frac{(C_0 - C_e)V}{W}. \quad (1)$$

Here, q_e is the adsorption capacity (mg g^{-1}) of the LCFA or LCFA-APTES at equilibrium, C_o and C_e (mg L^{-1}) are the initial and equilibrium concentrations of solute, V is the volume of the aqueous solution, and W is the mass in grams of the LCFA or LCFA-APTES.

The desorption of dyes was carried out by separately washing the dye (t = 5 min, T = 25°C) loaded adsorbents with 10 mL of 1 M NaOH (at pH = 12). The concentrations of desorbed dye in solutions were spectrophotometrically quantified.

2.6. Adsorption Isotherms. Adsorption of MO and XO onto LCFA and LCFA-APTES was investigated by two-parameter (Langmuir and Freundlich) and three-parameter (modified Langmuir–Freundlich, MLF) nonlinear models. In the Langmuir model, adsorption is assumed to be a dynamic and reversible process, meaning that the adsorbed molecules do not move on the surface, whereas they can go back to the solution. Each adsorbent sites have identical energy, and surface is made up of a single layer of molecules [38]. The nonlinear form of the Langmuir model is shown in Equation (2):

$$q_e = \frac{K_L q_{max} C_e}{1 + K_L C_e}, \quad (2)$$

where C_e is the equilibrium concentration of the adsorbate (mg L^{-1}), q_e is the amount of adsorbate adsorbed per unit amount of adsorbent at equilibrium (mg g^{-1}), and q_{max} (mg g^{-1}) and K_L (L mg^{-1}) are the maximum amount adsorbed and the Langmuir constants (function of energy of adsorption), respectively [31].

The dimensionless factor (R_L) can be used to predict the possibility of adsorption. The value of R_L indicates the direction of the isotherm to be either unfavorable ($R_L > 1$), favorable ($0 < R_L < 1$), or irreversible ($R_L = 0$) and can be estimated from Equation (3):

$$R_L = \frac{1}{K_L C_0 + 1}, \quad (3)$$

where C_o (mg L^{-1}) is the adsorbate initial concentration.

The Freundlich isotherm is suitable for heterogeneous surfaces. This model also takes into account lateral

Table 1: Chemical content of LCFA before and after surface activation measured by XRF.

Oxide wt % (excluding oxide compounds below 1%)	Pristine LCFA	After washing (distilled water at 50°C)	After surface activation (H_3PO_4 at 50°C for 1 h)
SiO_2	53.193	53.571	55.301
Al_2O_3	27.860	28.377	27.612
Fe_2O_3	7.018	6.400	6.161
K_2O	4.500	5.347	5.113
MgO	2.068	1.925	2.057
CaO	1.818	1.914	1.885
TiO_2	1.232	1.412	1.331

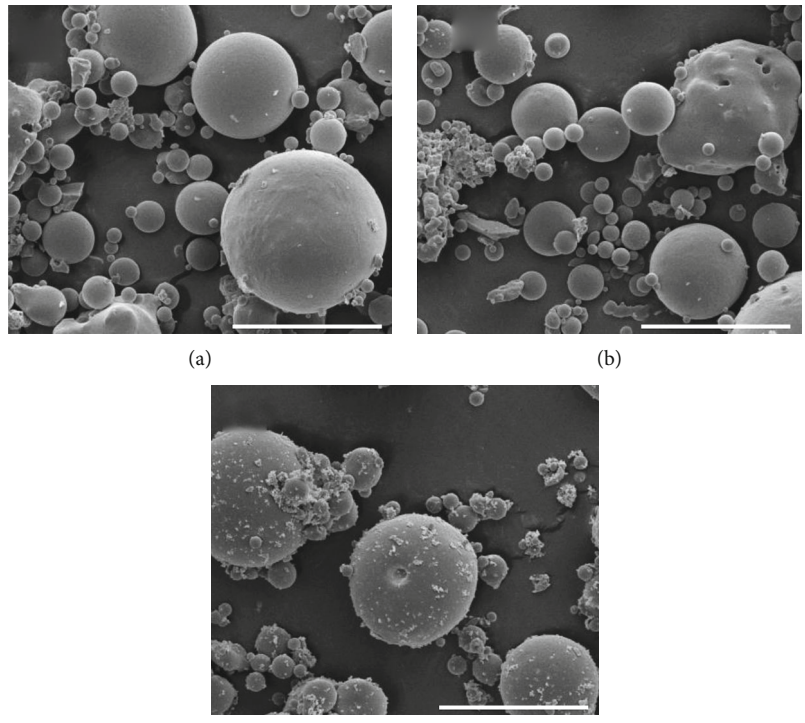

(a) (b) (c)

Figure 1: SEM images of (a) pristine LCFA, (b) activated LCFA, and (c) LCFA-APTES (scale bars: 20 μm).

interactions among adsorbed molecules. The nonlinear Freundlich equation as a function of concentration (C) can be mathematically represented by (Equation (4)):

$$q_e = K_f C_e^{\frac{1}{n}}, \tag{4}$$

where K_f is the Freundlich constant ($mg\,g^{-1}$), C_e is the concentration of adsorbate at equilibrium ($mg\,L^{-1}$) and the slop, $1/n$ with favorable range between 0 and 1. It is also measure of the relative distribution of the energy and surface heterogeneity.

The modified Langmuir–Freundlich (MLF) is a three-parameter empirical model. Since it is a combination of the Langmuir and Freundlich isotherms, it reduces to the Freundlich model at low adsorbate concentrations, while at high concentration, it transforms to the Langmuir model (Equation (5)).

$$q_e = \frac{q_{\text{mon}} K_{\text{MLF}} C_e^{1/n}}{1 + K_{\text{MLF}} C_e^{1/n}}, \tag{5}$$

where q_{mon} is the dye uptake capacity ($mg\,g^{-1}$), and K_{MLF} ($L\,mg^{-1}$) and n are the modified Langmuir–Freundlich (MLF) constants. The value of $1/n$ lies between zero and unity.

The sum of squares of residues (SSE) is used as error functions in order to determine the best adsorption isotherms and kinetic models (Equation (6)).

$$\text{SSE} = \frac{1}{m} \sum_{i=1}^{m} \left(q_{e,\text{pre}} - \mathrm{q}_{e,\text{exp}} \right)^2. \tag{6}$$

The computation tools of data-fitting for nonlinear form of Langmuir, Freundlich, and MLF adsorption isotherms as

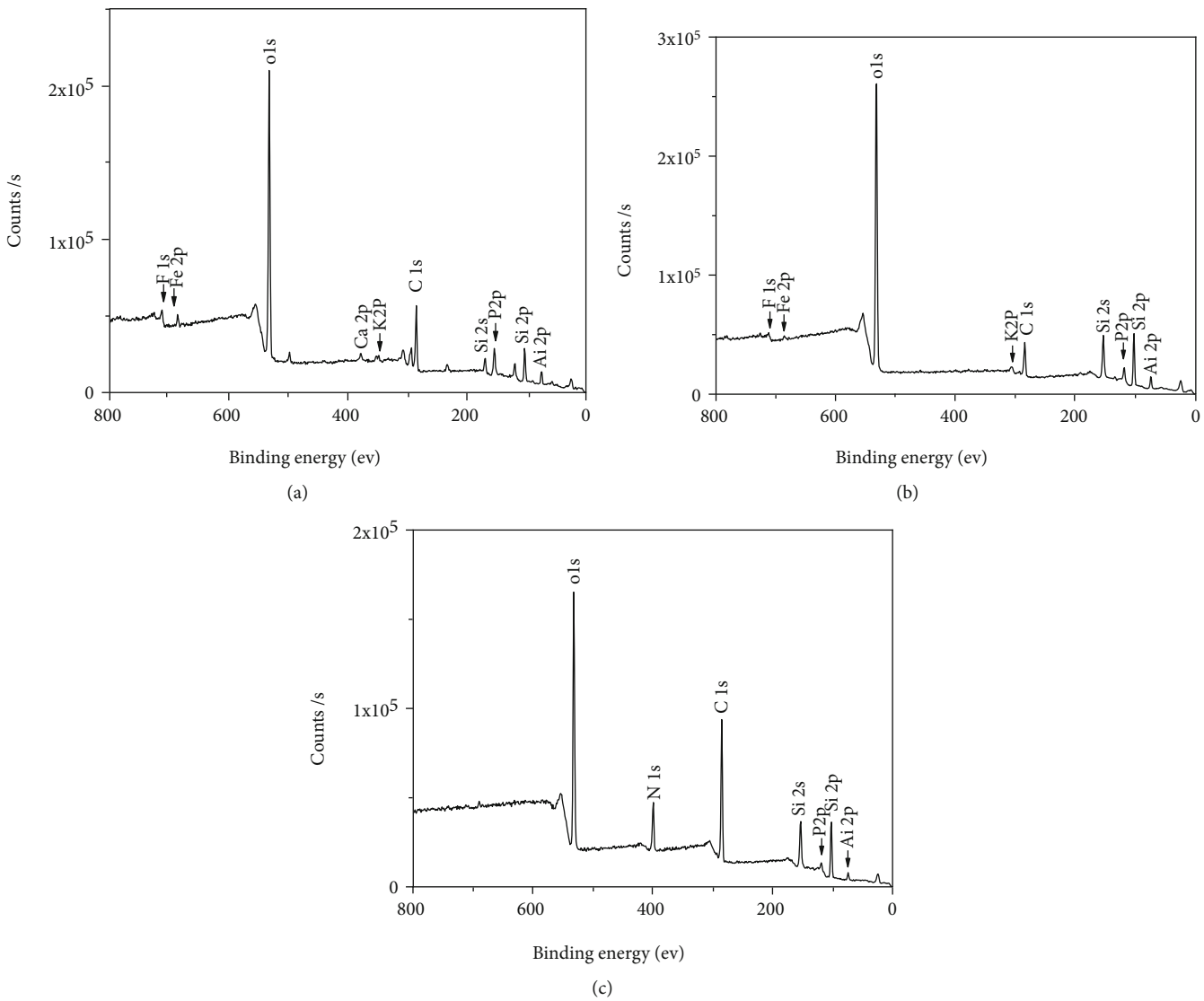

Figure 2: XPS survey scan of (a) pristine LCFA, (b) activated LCFA, and (c) LCFA-APTES.

well as adsorption kinetics models were employed with the support of MATLAB® R2019b.

2.7. Adsorption Kinetics. The kinetics analysis of the adsorption process is essential for having a preliminary information about the progress of adsorption and the maximum adsorbent capacity. The nonlinear pseudofirst-order model was described as in Equation (7):

$$q_t = q_e\left(1 - \exp^{-k_1 t}\right), \tag{7}$$

where q_e and q_t are the equilibrium and at time t adsorption capacities ($mg\,g^{-1}$), respectively, whereas k_1 is the pseudofirst-order rate constant of adsorption ($L\,min^{-1}$).

The nonlinear pseudosecond-order rate equation is as in Equation (8):

$$\boldsymbol{q_t = \frac{q_e^2 k_2 t}{1 + q_e k_2 t}}, \tag{8}$$

where the equilibrium adsorption capacity is q_e, and the pseudosecond-order rate constant is k_2 ($g\,mg^{-1}\,min^{-1}$).

3. Results and Discussion

3.1. Chemical and Structural Characterization of LCFA and LCFA-APTES. The chemical composition of the LCFA was analyzed with XRF before and after surface activation is given in Table 1. Since APTES also contains Si-O, XRF measurement was not conducted for LCFA-APTES. Surface activated LCFA has slightly higher SiO_2 compared to pristine LCFA, while other oxide compounds either remained unchanged or slightly decreased. According to XRD analysis results, approximately 89 wt% active sites ($SiO_2 + Al_2O_3 + Fe_2O_3$) are eligible for the adsorption study.

The specific surface area of the pristine and surface modified LCFAs measured with BET analysis and Figure S1 shows the N_2 adsorption-desorption isotherms of the fly ash samples. According to the IUPAC classification [39], all samples present a type IV adsorption isotherm with a

Table 2: Atomic percentages of the pristine and surface functionalized LCFA.

Sample	Atomic %								
	O 1 s	C 1 s	N 1 s	Si 2p	Al 2p	F 1 s	K 2p	P 2p	Fe 2p
Pristine LCFA	45.15	24.91	—	12.54	7.8	1.59	1.7	—	0.64
Activated LCFA	51.31	14.45	0.83	22.74	8.34	0.79	0.28	0.88	0.38
LCFA-APTES	30.28	40.49	8.91	15.9	3.78	0.64	—	—	—

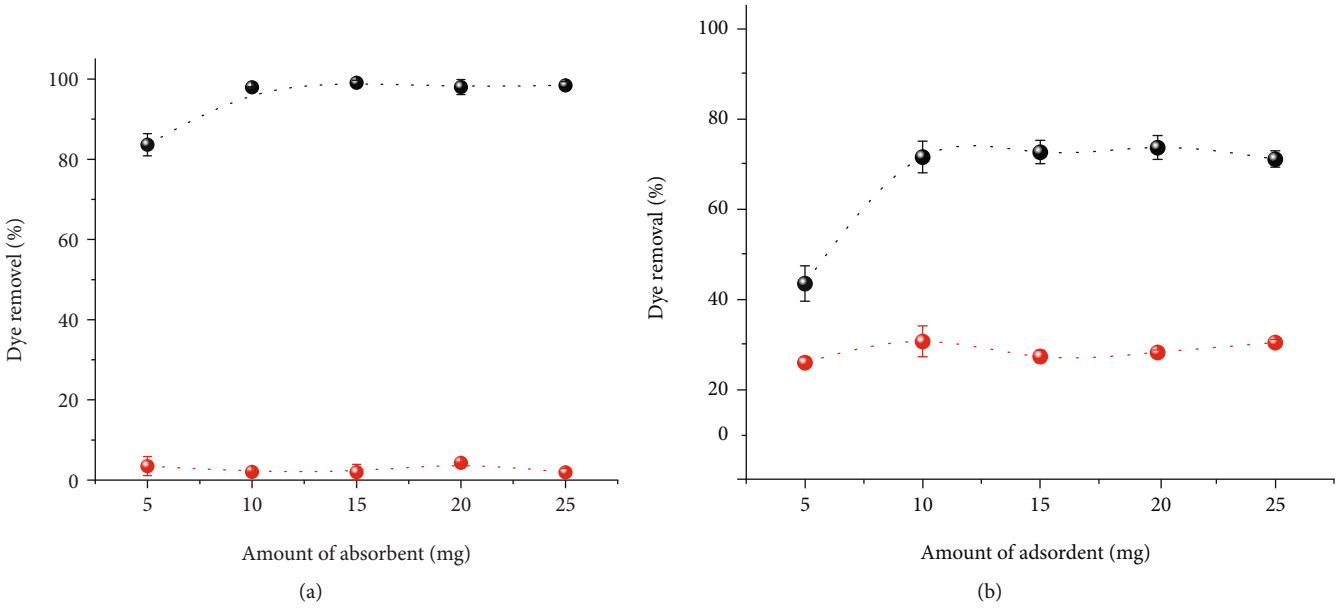

Figure 3: Effect of amount of adsorbent on dye removal percentage: (a) MO (pH = 4, t = 5 min, T = 25°C), (b) XO (pH = 4, t = 5 min, T = 25°C), removal by LCFA (red symbol), and LCFA-APTES (black symbol). The error bars represent the standard deviation of at least three repeated measurements.

type H3 hysteresis which does not completely close at low relative pressures (except washed fly ash). This indicates that the LCFAs have mesoporous characteristics. H3-type hysteresis curve, which is caused by capillary condensation in mesopores, indicates the formation of mesopores with slit-shaped cavities.

The activated LCFA has larger surface area (3.95 $m^2 g^{-1}$) followed by the pristine LCFA (2.97 $m^2 g^{-1}$) and LCFA-APTES (2.07 $m^2 g^{-1}$). The surface activation of fly ashes resulted in increased surface area in comparison to the washed pristine LCFA, indicating successful surface activation with the -OH group. The lower surface area of LCFA-APTES might be due to the fact that surface NH_2 groups can simply fill the small mesopores and restrict the access of N_2 to the pores at liquid nitrogen temperature [40, 41]. It is clearly seen that the N_2 adsorption resulting from the filling of small pores is considerably reduced in the P/P_0 range of 0–0.2 (Figure S1e).

The morphology of LCFAs was investigated by SEM which reveals smooth spherical particles (Figure 1 and Figure S2). The LCFA has very broad particle size, and size distribution was calculated using ImageJ® counting particles in the 100 μm^2 area. Particle diameter was ranging from 0.5 to 14 μm, and the average diameter was 2.23 ± 2.17 μm (Figure S2). Washing and acid activation steps (Figures S2b and S2c) ensure that the particles were still in spherical shape, and size does not change significantly; only some water-soluble impurities were removed. Furthermore, grafting of APTES on the LCFA surface did not change the dimensional size and shape of the particles (Figures 1(a) and 1(c)). The thickness of APTES layer was hard to determine from SEM analysis.

In order to better probe the surface composition of LCFAs before and after APTES layer formation, energy dispersive X-ray spectroscopy (EDX) and XPS were employed. According to EDX analysis results (Table S1), the oxygen content of both pristine and active LCFA is quite high (44.12 and 60.22%, respectively), whereas it decreases by almost half after the silanization. In contrast, the Si content increased slightly after the surface modification, which is due to extra Si atom from the silane molecule. In addition, two new elements (C and N) were observed in LCFA-APTES, which belong to the silane molecule. Elemental composition is further investigated by XPS and bonding of the functional groups on LCFA, and the results are shown in Figure 2 and Table 2. The survey scan of LCFA-APTES indicated signals at 152.4 and 102.23 eV, which belong to the binding energy of Si2s and Si2p orbitals. The signal for N1s was observed at 399.3 eV in the survey scan of LCFA-APTES confirms the amine functionalization, while pristine LCFA did not show any presence of signals for N orbitals (Figure 2(a)), whereas the signal for the C1s and

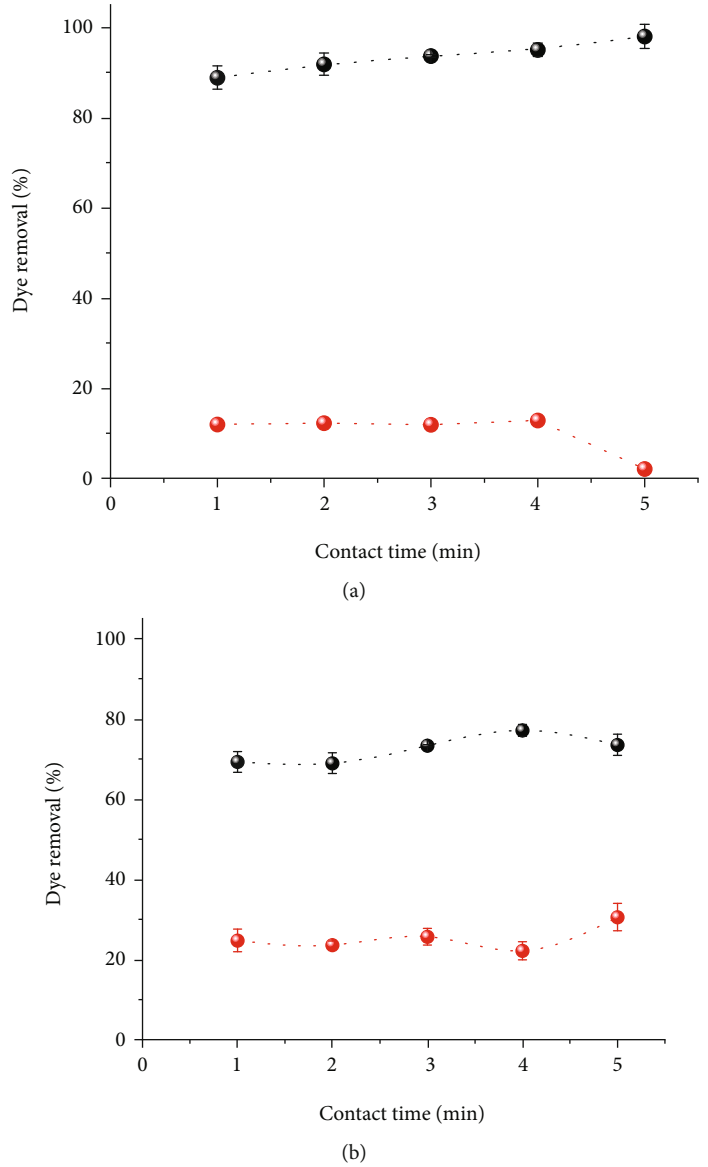

Figure 4: Effect of contact time on dye removal percentage: (a) MO (pH = 4, T = 25°C, amount of adsorbent 10 mg) and (b) XO (pH = 4, T = 25°C, amount of adsorbent 20 mg) by LCFA (red symbol) and LCFA-APTES (black symbol). The error bars represent the standard deviation calculated from at least three repeated measurements for each contact time.

O1s orbitals of the carbon and oxygen contents of LCFA-APTES was identified at 284.89 and 531.91 eV (Figure 2(b)). The success of immobilization process was determined by a change in the N/C atomic ratio (Table 2). Comparison of elemental compositions between EDX and XPS may not be healthy. Because while EDX analyses is local, XPS gives more detailed and reliable results because it contains the average of three different regions on the sample. On the other hand, we can compare the trends of the change of elemental content before and after surface treatments. In this context, the first thing that stands out in both analyses is the decrease in oxygen content by silanization, because the organic coating placed on the surface covers the oxide surface. Another similarity is the increasing amounts of N and Si elements after the silanization. In this respect, both techniques yielded consistent results.

TGA analysis performed to compare the amount of APTES layer on the LCFA surface (Figure S3). LCFA-APTES samples showed slight weight loss (~1.15% at 800°C, respectively). After achieving surface functionalization on LCFA, the adsorption performance of LCFA-APTES was tested against two anionic dyes (MO and XO) using batch procedures.

3.2. Effect of Adsorbent Quantity. The effect of adsorbent dose on the anionic dye adsorption was studied at 25°C with LCFA particles of various amounts (5, 10, 15, 20, and 25 mg) using 10 mL of 15 ppm dye solutions at pH = 7. MO almost did not adsorb on LCFA in all adsorbent doses and LCFA and did not show any correlation between the increasing amount of adsorbent and adsorption capacity (Figure 3(a)), whereas LCFA-APTES attained to its maximum adsorption

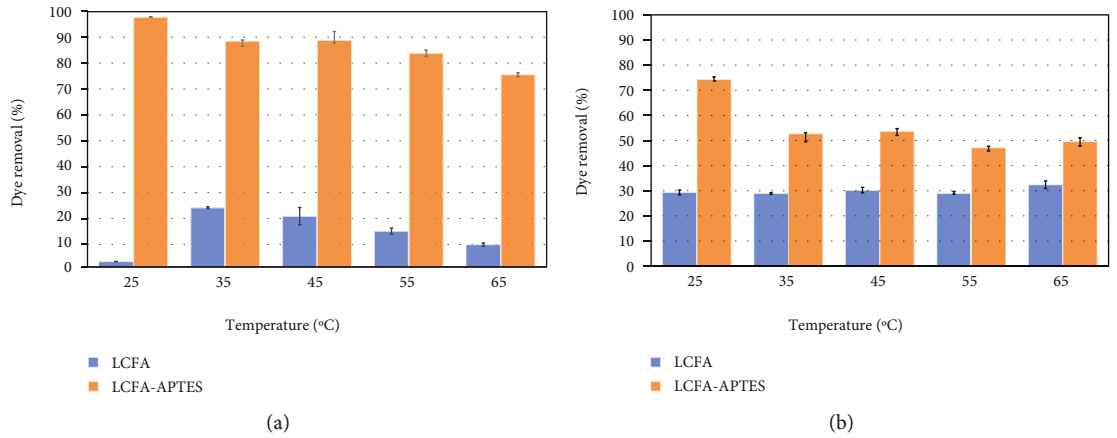

Figure 5: Effect of temperature on dye removal percentage: (a) MO (pH = 4, t = 5 min, amount of adsorbent 10 mg) and (b) XO (pH = 4, t = 5 min, amount of adsorbent 20 mg) by LCFA and LCFA-APTES. The error bars represent the standard deviation of at least three repeated measurements at each temperature value.

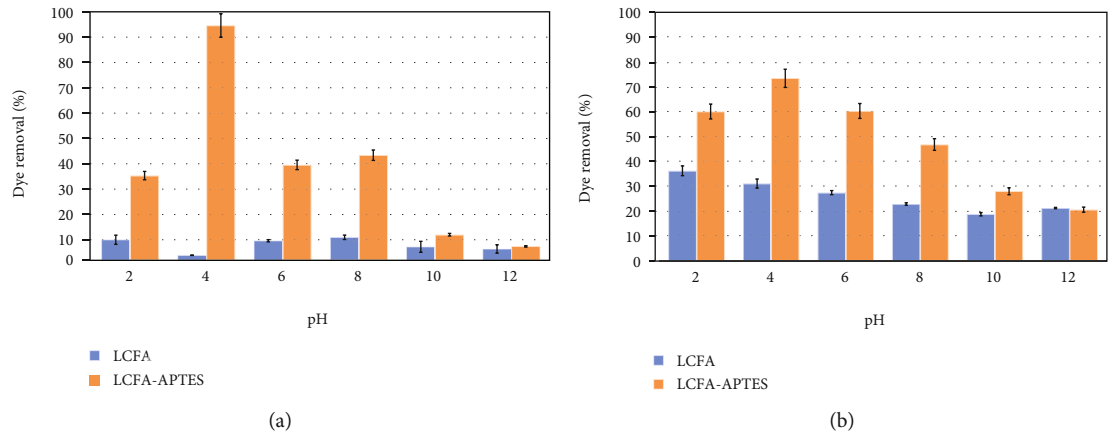

Figure 6: Effect of pH on dye removal percentage: (a) MO (t = 5 min, T = 25°C, amount of adsorbent 10 mg) and (b) XO (t = 5 min, T = 25°C, amount of adsorbent 20 mg) by LCFA and LCFA-APTES. The error bars represent the standard deviation of at least three repeated measurements at each pH value.

capacity of 98% at 10 mg for MO (Figure 3). The adsorption mechanisms of dyes on adsorbents are likely to be the ionic interactions between negative groups of the dyes (SO_3^- and COO^-) and the amine groups (NH_2-) at this pH. Because the amine groups are protonated at acidic condition, the net charge of LCFA-APTES is positive. The charge states of the samples were measured with zeta potential and reported in Table S2. In addition to electrostatic interaction, the adsorption of MO and XO dyes onLCFA-APTES might also governed by H-bonds between dye molecules and APTES.

It was also observed that LCFA-APTES is more selective in MO adsorption against XO as adsorption capacity at 10 mg is 98% for MO and 75% for XO. The better adsorption capacity of MO over XO can be explained by size effect [42]. MO has a very small molecular size (1.2 nm) compared to XO facilitating dye molecules to be packed more closely on the LCFA [43]. Hence, such small molecular size might improve the diffusion of MO that leads to higher mass transfer rate from bulk to the boundary layer around the LCFA particle surface. Besides, the monovalent nature of MO enables one to one interaction among ionic groups, while bulkier XO reduces the electrostatic interaction of adjacent ionic groups with amine groups on the adsorbent surface.

3.3. Effect of Contact Time. The optimum contact time was determined adding 10 mg for MO and 20 mg for XO to 10 mL of 15 ppm dye solutions for time durations ranging from 1 to 5 min at pH = 4. The maximum % age of dye remove was obtained between 4 and 5 min for both dyes. The adsorption efficiency of LCFA-APTES was increasing with time, while pristine LCFA did not show significant change until 4 min (Figure 4). The maximum adsorption of LCFA-APTES was 98% for MO and 75% for XO, whereas for pristine LCFA, maximum capacity was 13% for MO and 26% for XO.

3.4. Effect of Temperature. It is well known that temperature is the most important adsorption parameter. To investigate the influence of temperature on the LCFA adsorption

Table 3: Performance evaluation of LCFA-APTES with aforementioned adsorbents for MO dye adsorption as a function of maximum adsorption capacity, equilibrium time, and medium pH.

Adsorbent	Adsorption capacity (mg g^{-1})	Equilibrium time (min)	Solution pH	Reference
Muscovite_supported Fe_3O_4 nanoparticles	149.25	75	3.0	[10]
Mn–rich synthetic mica	107.3	120	3.0	[47]
ZnO-PANI nanocomposite	240.84	15	4.0	[48]
Multiwalled carbon nanotubes	64.7	120	2.3	[49]
Protonated crosslinked chitosan	89.30	720	3.0	[50]
Aminated pumpkin seed powder (APSP)	200.30	60	3.0	[45]
Calcined Lapindo volcanic mud	333.3	30	3.0	[51]
Bottom ash	3.618	240	3.0	[46]
LCFA-APTES	17.91	1-2	4.0	Current study

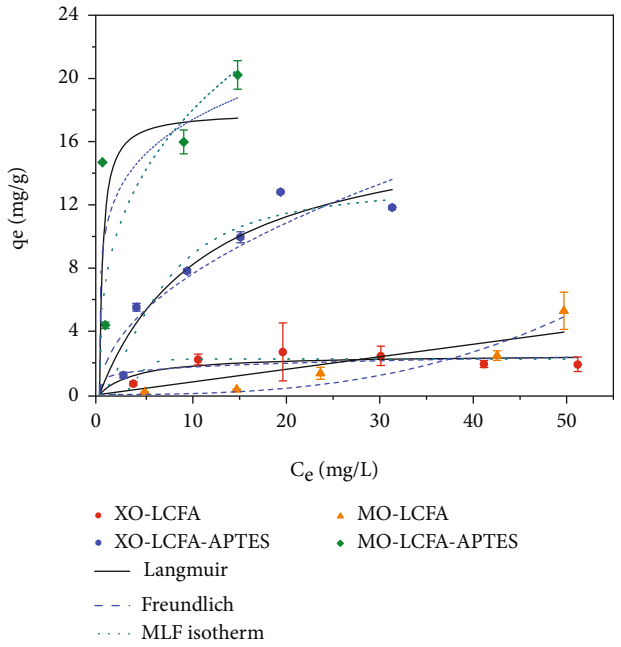

Figure 7: Adsorption isotherms and nonlinear curve fits of Langmuir (black solid line), Freundlich (blue dash line), and MLF (black dots)) for XO-LCAFA (red circle), XO-LCFA APTES (blue hexagon), MO-LCFA (orange triangle), and MO-LCFA APTES (green diamond), respectively. The error bars show the standard deviation of at least three repeated measurements.

Table 4: Adsorption isotherm parameters of MO and XO removed by LCFA and LCFA-APTES.

	Parameters	MO	XO
LCFA			
Langmuir	q_{max} (mg g^{-1})	740.683	3.250
	R_L	619.831	1.269
	SSE	7.977	0.116
Freundlich	K_f (mg g^{-1})	9.65x10^{-5}	1.122
	1/n	2.766	0.189
	SSE	0.214	0.158
MLF	K_{MLF} (L g^{-1})	2.28x10^{-4}	1.35x10^{-4}
	q_{mon} (mg g^{-1})	946.535	2.238
	1/n	0.719	6.274
	SSE	0.502	0.057
LCFA-APTES			
Langmuir	q_{max} (mg g^{-1})	17.906	14.723
	R_L	0.924	0.786
	SSE	1.994	0.641
Freundlich	K_f (mg g^{-1})	11.222	2.394
	1/n	0.191	0.504
	SSE	8.593	0.921
MLF	K_{MLF} (L g^{-1})	0.005	0.046
	q_{mon} (mg g^{-1})	1.64x10^{3}	13.253
	1/n	0.3423	1.642
	SSE	21.703	0.8506

performance, temperature is varied between 25°C and 65°C systematically. Equal amounts of adsorbents (10 mg for MO and 20 mg for XO) were employed into 10 mL and 15 ppm dye solutions. No correlation with temperature was observed for MO adsorption on pristine LCFA. Adsorption performance of XO remained almost the same when the temperature is increased. For LCFA APTES, although MO showed higher adsorption capacity in all temperature ranges, gradual decrease in adsorption was observed as temperature increased for both dyes (Figure 5). The maximum percentage of dye removal was observed at room temperature with LCFA-APTES (98% for MO and 75% for XO). The better adsorption at low temperature might also indicate the exothermic nature of the interaction; even so, the mobility of the dye molecule decreases with decreasing temperature. This trend indicates that interaction between dyes and adsorbents is a physical adsorption rather than chemisorption. Parida et al. [44] demonstrated that the solubility limits commonly decrease with the increase in temperature and reduces the adsorption capacity preventing the physical interactions between dyes and adsorbents.

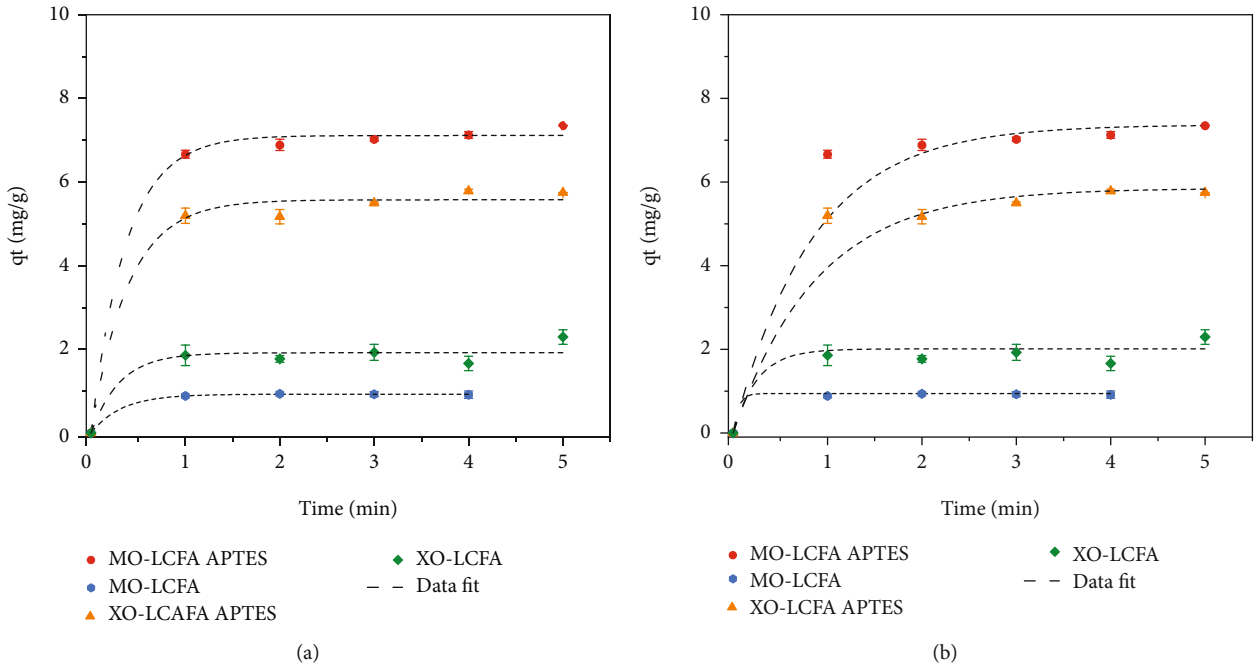

Figure 8: Adsorption kinetic and nonlinear curve fits (black dash line) of (a) pseudofirst-order and (b) pseudosecond-order kinetics for the adsorption of MO-LCFA APTES (red circle), MO-LCFA (blue hexagon), XO-LCFA APTES (orange triangle), and XO-LCFA (green diamond). The error bars represent the standard deviation of at least three repeated measurements for each time value.

3.5. Effect of pH. Solution pH value is a governing parameter to control adsorption capacity when adsorption mechanism is based on ionic interaction. pH variation accounts for the degree of ionization of the dyes and the nature of the adsorbent surface charge groups. The solution pH range varied between 2 and 12 using 0.1 M HCl and 0.1 M NaOH. The adsorption capacity of LCFA-APTES initially raised as pH switched from 2 to 4 (Figure 6). The maximum adsorption capacity of LCFA-APTES was obtained at pH = 4 for each dye (98% for MO and 76% for XO). More increase in pH led to a reduction in the efficiency of the adsorbents.

After all these parameters are optimized, the adsorption performance of LCFA-APTES has been compared with similar adsorbents for the removal of MO dye as regards of maximum adsorption capacity (mg. g^{-1}), equilibrium time (min), and solution pH as shown in Table 3. Almost all these adsorbents showed their highest performance at low pH conditions (pH ~2-4). It is seen that ZnO-PANI nanocomposite has the highest MO adsorption capacity (240.84 mg.g^{-1}) [10]. Aminated pumpkin seed powder (APSP) has also superior adsorption capacity while equilibrium time of adsorption is around 1 h [45]. This study and the other fly ash [46] obtained from natural resources gave the lowest adsorption capacity. Overall, the adsorption capacity of the synthetic adsorbents is higher than natural ones. However, one of the most important advantages of this study is that it has a very short adsorption time (1-2 min).

3.6. Adsorption Isotherms. Three traditional adsorption models were used to calculate the mechanism and capacity of adsorbents towards selected dyes. Langmuir and Freundlich adsorption models which are so far most frequently

Table 5: Kinetic analysis results for the adsorption of MO and XO on LCFA and LCFA-APTES.

	Parameters	MO	XO
LCFA			
Pseudo-first-order	q_e (mg g^{-1}) experimental	0.740	2.201
	q_e (mg g^{-1}) calculated	0.924	1.916
	k_1 (min^{-1})	3.294	3.100
	SSE	2.03×10^{-5}	0.010
Pseudo-second-order	q_e (mg g^{-1}) experimental	0.740	2.201
	q_e (mg g^{-1}) calculated	0.942	2.008
	k_2 (g/mg min)	17.737	3.951
	SSE	4.95×10^{-4}	0.016
LCFA-APTES			
Pseudo-first-order	q_e (mg g^{-1}) experimental	7.350	5.752
	q_e (mg g^{-1}) calculated	7.111	5.574
	k_1 (min^{-1})	2.710	2.544
	SSE	0.006	0.031
Pseudo-second-order	q_e (mg g^{-1}) experimental	7.350	5.752
	q_e (mg g^{-1}) calculated	7.368	5.849
	k_2 (g/mg min)	1.188	1.126
	SSE	0.412	0.262

Table 6: Thermodynamic parameters for the adsorption of MO and XO on LCFA and LCFA-APTES.

Parameters (kJ Mol^{-1})	XO	MO
LCFA		
ΔG°	3.79 ± 0.4	3.06 ± 0.11
ΔH°	1.37 ± 1.17	−33.28 ± 2.77
ΔS°	−0.01 ± 0.003	−0.12 ± 0.01
LCFA-APTES		
ΔG°	−0.83 ± 0.34	−9.62 ± 0.19
ΔG°	−20.15 ± 2.02	−50.40 ± 2.91
ΔG°	−0.07 ± 0.01	−0.07 ± 0.01

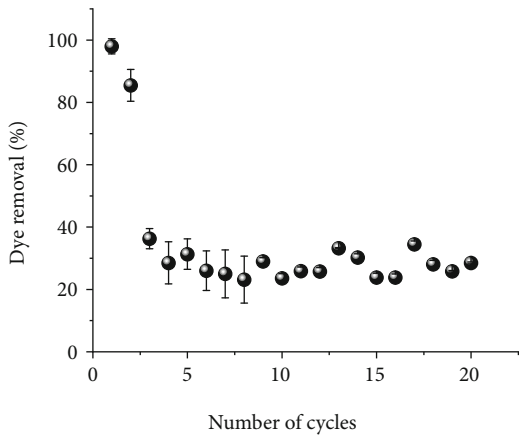

Figure 9: Reusability of LCFA-APTES for the adsorption of MO (pH = 4 for adsorption and pH = 12 for desorption, $T = 25^{\circ}$C, $t =$ 5 min, amount of adsorbent = 10 mg). The error bars represent the standard deviation of at least three repeated measurements for each cycle.

used isotherms are two-parameter models, while modified Langmuir-Freundlich (MLF) is a three-parameter empirical model (Figure 7). All models were fitted to experimental values in nonlinear form to minimize the error function. The least-square regression based on the sum of squares of residues (SSE) is employed as error functions in order to find the best adsorption isotherms and kinetic models. A comparison of the three isotherms is given in Table 4.

Adsorption data of XO on pristine LCFA cannot fit to any isotherms physically meaningfully since $R_L > 1$ and $n > 1$ which is indication of unfavorable isotherm, whereas MO adsorption on LCFA is fitted best with Freundlich ($n < 1$ and lowest SSE). The adsorption of MO and XO on LCFA-APTES is better projected by the Langmuir model. The maximum adsorption capacities of LCFA-APTES for MO and XO dyes were calculated as 17.91 and 14.72 mg g^{-1}, respectively. Incoherent adsorption parameters for MO adsorption on LCFA clearly show that there is no specific interaction between LCFA and MO.

3.7. Adsorption Kinetics. Kinetics of the adsorption process gives useful information about the adsorbate-adsorbent interaction and the adsorption rate. In order to investigate the kinetic effect, pseudofirst-order and pseudosecond-order kinetic models were employed (Figure 8), and the corresponding rate constants are given in Table 5.

The SSE values indicated that the adsorption of dyes proceeded by the pseudofirst-order kinetic model. Adsorption of both dyes on LCFA has slightly faster rate than LCFA-APTES ($k_1 = 3.294$ min^{-1} for MO and $k_1 = 3.100$ min^{-1} for XO). In addition, the calculated and experimental values of q_e were found to be compatible with each other.

3.8. Adsorption Thermodynamics. The adsorption process is complemented by evolution of heat and temperature that might have negative or positive effect depending on interaction type between adsorbate and adsorbent molecules. The thermodynamic parameters such as the Gibbs' free energy (ΔG°), the standard enthalpy change (ΔH°), and the standard entropy change (ΔS°) were conducted to study the effect of temperature on the adsorption process [38, 52–54]. The magnitude of Gibbs energy of adsorption (ΔG°) was calculated from Equations (9) and (10):

$$\Delta G = -\mathrm{RT}\ln \mathrm{K}_c, \tag{9}$$

where

$$K_c = \frac{q_e}{C_e}, \tag{10}$$

where K_c is the equilibrium constant in solution, (mg L^{-1}), T is the absolute temperature (K), and R is the gas constant (8.314 J/mol K).

The enthalpy changes ΔH° and ΔS° were obtained from van't Hoff equation (Equation (11)):

$$\ln \mathrm{K}_c = \frac{\Delta S}{R} - \frac{\Delta H}{\mathrm{RT}} \tag{11}$$

The calculated thermodynamic parameters are summarized in Table 6. The negative values of ΔG° confirmed that the adsorption of dyes on LCFA-APTES is spontaneous, while the negative values of ΔH° indicated the exothermic nature of adsorption activities. The negative ΔS° showed a restriction in the freedom of molecular movement after the adsorption.

3.9. Reusability Studies. The recycling ability of an adsorbent is a key determinant for the economic viability of the product. To examine the reusability, dye loaded LCFAs were washed with ethanol before each adsorption and desorption cycle. Desorption processes were carried out via employing 1 M NaOH (pH = 12). Both adsorbents (LCFA-APTES) showed the best performance in terms of reusability against MO dye. The MO dye removal efficiency declined steadily for both adsorbents up to 3 cycles. After 5 cycles, % removal efficiencies oscillate between 20% and 30% (Figure 9).

4. Conclusions

In this study, we showed that one can use an undesirable residue of thermal power plants as a cheap nano/microparticle

source with a high surface area, to hold toxic dyes that are also classified as hazardous waste for the environment. To demonstrate it, lignite coal fly ash was functionalized with 3-aminopropyltriethoxysilane (LCFA-APTES). Then, it was exploited as an inexpensive adsorbent for the effective removal of widely used textile dyes (MO and XO) from aqueous solutions. The adsorption capacity of developed materials was compared with its nonfunctionalized counterpart. The LCFA-APTES has the maximum adsorption capacity of 17.91 mg g^{-1} for MO and 14.72 mg g^{-1} for XO. It also showed very short reaction time, since the adsorption equilibrium (98% for MO and 75% for XO) was achieved less than 5 min. These results indicated that adsorption performance of LCFA-APTES is better than pristine LCFA. The interaction between dye molecules (MO and XO) and LCFA-APTES is governed by electrostatic forces and hydrogen bonding. The ionic interactions occur between negative groups of the dyes (SO_3^- and COO^-) and the amine groups (NH_2-) at pH = 4.0, since the amine groups are protonated at acidic condition and the net charge of LCFA-APTES is positive. In addition to electrostatic interaction, the adsorption of MO and XO dyes onto LCFA-APTES might also governed by H-bonds between dye molecules and APTES.

Overall, the present study demonstrates a simple and cost-effective route for the environmental remediation with amine-functionalized lignite coal fly ash. Although the adsorption time of this study is ideal for practical applications, the maximum adsorption capacity still needs to be improved. Furthermore, it is inconvenient to use freely moving fly ash particles in water purification. For this purpose, our future plan is to grow aminated polymer brushes on the LCFA surface and prepare an aerogel membrane in which fly ash particles are bonded and aims to test it for water treatment in the real environment.

Data Availability

Some data is provided in the Supplementary Information files that submitted alongside their manuscript. The MATLAB code for nonlinear curve fits will be provided upon request.

Disclosure

Senem Çitoğlu current address is Acıbadem Mehmet Ali Aydınlar University, Biomaterials Center, Ataşehir, İstanbul, 34684, Turkey.

Conflicts of Interest

The authors declare that there is no conflict of interest regarding the publication of this paper.

Acknowledgments

H.D. gratefully acknowledges Max–Planck–Gesellschaft (MPG) for the financial support of the MPIP-TOBB ETU Partner Group Program (Soft Matter in Nanoconfinement). We are grateful to members of the UNAM, Bilkent University, for their enduring support and helpfulness. Also, Thanks are due to Borçelik Steel Industry Inc. for their support to use SEM and EDX analyses. Gratefully acknowledges Eczacıbaşı Building Products (Vitra) for their support to obtain textile dyes.

Supplementary Materials

Figure S1: N_2 adsorption-desorption isotherms of fly ash samples at 77 K: (a) pristine LCFA, (b) activated-LCFA, and (c) LCFA-APTES. Figure S2: SEM images of (a) pristine LCFA, (b) after washing with distilled water at 50°C, and (c) after acid (H_3PO_4) treatment. Figure S3: TGA curves of the LCFAs. Table S1: EDX elemental analysis of the pristine and surface functionalized LCFA. Table S2: zeta potential measurement results of the pristine and surface functionalized LCFA. *(Supplementary Materials)*

References

[1] Z. T. Ahmed and D. W. Hand, "Direct adsorption isotherms of AEAs and fly ash: α-olefin sulfonate and combination admixtures," *ACS Sustainable Chemistry & Engineering*, vol. 3, no. 2, pp. 216–223, 2015.

[2] S. Jin, Z. Zhao, S. Jiang, J. Sun, H. Pan, and L. Jiang, "Comparison and summary of relevant standards for comprehensive utilization of fly ash at home and abroad," *IOP Conference Series: Earth and Environmental Science*, vol. 621, no. 12006, pp. 1–5, 2021.

[3] O. Özdemir and M. S. Çelik, "Characterization and recovery of lignitic fly ash byproducts from the Tuncbilek Power Station," *Canadian Metallurgical Quarterly*, vol. 41, no. 2, pp. 143–150, 2002.

[4] "2012 Coal combustion product production & use survey report," March 2014, http://www.acaa-usa.org/Portals/9/Files/PDFs/revisedFINAL2012CCPSurveyReport.pdf.

[5] V. Somerset, L. Petrik, and E. Iwuoha, "Alkaline hydrothermal conversion of fly ash filtrates into zeolites 2: utilization in wastewater treatment," *Journal of Environmental Science and Health, Part A*, vol. 40, no. 8, pp. 1627–1636, 2005.

[6] K. Zhao, Y. Hu, Y. Tian, D. Chen, and Y. Feng, "Chlorine removal from MSWI fly ash by thermal treatment: effects of iron/aluminum additives," *Journal of Environmental Sciences*, vol. 88, pp. 112–121, 2020.

[7] M. Ahmaruzzaman, "Role of fly ash in the removal of organic pollutants from wastewater," *Energy & Fuels*, vol. 23, no. 3, pp. 1494–1511, 2009.

[8] S. Dogar, S. Nayab, M. Q. Farooq et al., "Utilization of biomass fly ash for improving quality of organic dye-contaminated water," *ACS Omega*, vol. 5, no. 26, pp. 15850–15864, 2020.

[9] B. Lellis, C. Z. Fávaro-Polonio, J. A. Pamphile, and J. C. Polonio, "Effects of textile dyes on health and the environment and bioremediation potential of living organisms," *Biotechnology Research and Innovation*, vol. 3, no. 2, pp. 275–290, 2019.

[10] M. A. Barakat, R. Kumar, E. C. Lima, and M. K. Seliem, "Facile synthesis of muscovite-supported Fe_3O_4 nanoparticles as an adsorbent and heterogeneous catalyst for effective removal of methyl orange: Characterisation, modelling, and mechanism," *Journal of the Taiwan Institute of Chemical Engineers*, vol. 119, pp. 146–157, 2021.

[11] A. Farrukh, A. Akram, A. Ghaffar et al., "Surface-functionalized silica gel adsorbents for efficient remediation of cationic dyes," *Pure and Applied Chemistry*, vol. 86, no. 7, pp. 1177–1188, 2014.

[12] T. Robinson, G. McMullan, R. Marchant, and P. Nigam, "Remediation of dyes in textile effluent: a critical review on current treatment technologies with a proposed alternative," *Bioresource Technology*, vol. 77, no. 3, pp. 247–255, 2001.

[13] E. Forgacs, T. Cserháti, and G. Oros, "Removal of synthetic dyes from wastewaters: a review," *Environment International*, vol. 30, no. 7, pp. 953–971, 2004.

[14] A. K. Verma, R. R. Dash, and P. Bhunia, "A review on chemical coagulation/flocculation technologies for removal of colour from textile wastewaters," *Journal of Environmental Management*, vol. 93, no. 1, pp. 154–168, 2012.

[15] C. A. Martínez-Huitle and E. Brillas, "Decontamination of wastewaters containing synthetic organic dyes by electrochemical methods: a general review," *Applied Catalysis B: Environmental*, vol. 87, no. 3-4, pp. 105–145, 2009.

[16] V. K. Gupta and Suhas, "Application of low-cost adsorbents for dye removal - A review," *Journal of Environmental Management*, vol. 90, no. 8, pp. 2313–2342, 2009.

[17] Y. Anjaneyulu, N. Sreedhara Chary, and D. Samuel Suman Raj, "Decolourization of industrial effluents–available methods and emerging technologies – a review," *Reviews in Environmental Science and Bio/Technology*, vol. 4, no. 4, pp. 245–273, 2005.

[18] M. T. Yagub, T. K. Sen, S. Afroze, and H. M. Ang, "Dye and its removal from aqueous solution by adsorption: a review," *Advances in Colloid and Interface Science*, vol. 209, pp. 172–184, 2014.

[19] C. Z. Liang, S.-P. Sun, F.-Y. Li, Y.-K. Ong, and T.-S. Chung, "Treatment of highly concentrated wastewater containing multiple synthetic dyes by a combined process of coagulation/flocculation and nanofiltration," *Journal of Membrane Science*, vol. 469, pp. 306–315, 2014.

[20] J. Wu, M. A. Eiteman, and S. E. Law, "Evaluation of membrane filtration and ozonation processes for treatment of reactive-dye wastewater," *Journal of Environmental Engineering*, vol. 124, no. 3, pp. 272–277, 1998.

[21] Q. H. Hu, S. Z. Qiao, F. Haghseresht, M. A. Wilson, and G. Q. Lu, "Adsorption study for removal of basic red dye using bentonite," *Industrial and Engineering Chemistry Research*, vol. 45, no. 2, pp. 733–738, 2006.

[22] T. L. Silva, A. Ronix, O. Pezoti et al., "Mesoporous activated carbon from industrial laundry sewage sludge: adsorption studies of reactive dye remazol brilliant blue R," *Chemical Engineering Journal*, vol. 303, pp. 467–476, 2016.

[23] E. Lorencgrabowska and G. Gryglewicz, "Adsorption characteristics of Congo red on coal-based mesoporous activated carbon," *Dyes and Pigments*, vol. 74, no. 1, pp. 34–40, 2007.

[24] S. Nayab, H. Baig, A. Ghaffar et al., "Silica based inorganic–organic hybrid materials for the adsorptive removal of chromium," *RSC Advances*, vol. 8, no. 42, pp. 23963–23972, 2018.

[25] T. R. Barbosa, E. L. Foletto, G. L. Dotto, and S. L. Jahn, "Preparation of mesoporous geopolymer using metakaolin and rice husk ash as synthesis precursors and its use as potential adsorbent to remove organic dye from aqueous solutions," *Ceramics International*, vol. 44, no. 1, pp. 416–423, 2018.

[26] I. D. Mall, V. C. Srivastava, and N. K. Agarwal, "Removal of Orange-G and Methyl Violet dyes by adsorption onto bagasse fly ash –kinetic study and equilibrium isotherm analyses," *Dyes and Pigments*, vol. 69, no. 3, pp. 210–223, 2006.

[27] V. K. Gupta, A. Mittal, V. Gajbe, and J. Mittal, "Removal and recovery of the hazardous azo dye acid orange 7 through adsorption over waste materials: bottom ash and de-oiled soya," *Industrial and Engineering Chemistry Research*, vol. 45, no. 4, pp. 1446–1453, 2006.

[28] R. K. Ghosh and D. D. Reddy, "Crop residue ashes as adsorbents for basic dye (methylene blue) removal: adsorption kinetics and Dynamics," *Clean Soil Air Water*, vol. 42, no. 8, pp. 1098–1105, 2014.

[29] N. A. Rashidi and S. Yusup, "Overview on the potential of coal-based bottom ash as low-cost adsorbents," *ACS Sustainable Chemistry & Engineering*, vol. 4, no. 4, pp. 1870–1884, 2016.

[30] N. Koshy and D. N. Singh, "Fly ash zeolites for water treatment applications," *Journal of Environmental Chemical Engineering*, vol. 4, no. 2, pp. 1460–1472, 2016.

[31] G. Chandrasekar and W.-S. Ahn, "Synthesis of cubic mesoporous silica and carbon using fly ash," *Journal of Non-Crystalline Solids*, vol. 354, no. 33, pp. 4027–4030, 2008.

[32] D. Li, H. Min, X. Jiang, X. Ran, L. Zou, and J. Fan, "One-pot synthesis of aluminum-containing ordered mesoporous silica MCM-41 using coal fly ash for phosphate adsorption," *Journal of Colloid and Interface Science*, vol. 404, pp. 42–48, 2013.

[33] S. Nayab, A. Farrukh, Z. Oluz et al., "Design and fabrication of branched polyamine functionalized mesoporous silica: an efficient absorbent for water remediation," *ACS Applied Materials & Interfaces*, vol. 6, no. 6, pp. 4408–4417, 2014.

[34] F. Hoffmann, M. Cornelius, J. Morell, and M. Fröba, "Silica-based mesoporous organic–inorganic hybrid materials," *Angewandte Chemie International Edition*, vol. 45, no. 20, pp. 3216–3251, 2006.

[35] N. Linares, E. Serrano, M. Rico et al., "Incorporation of chemical functionalities in the framework of mesoporous silica," *Chemical Communications*, vol. 47, no. 32, pp. 9024–9035, 2011.

[36] L. C. Hu and K. J. Shea, "Organo–silica hybrid functional nanomaterials: how do organic bridging groups and silsesquioxane moieties work hand-in-hand?," *Chemical Society Reviews*, vol. 40, no. 2, pp. 688–695, 2011.

[37] S. Fujita and S. Inagaki, "Self-organization of organosilica solids with molecular-scale and mesoscale periodicities," *Chemistry of Materials*, vol. 20, no. 3, pp. 891–908, 2008.

[38] M. Y. Nassar, E. I. Ali, and E. S. Zakaria, "Tunable autocombustion preparation of TiO2nanostructures as efficient adsorbents for the removal of an anionic textile dye," *RSC Advances*, vol. 7, no. 13, pp. 8034–8050, 2017.

[39] Z. A. ALOthman, "A review: fundamental aspects of silicate mesoporous materials," *Maternité*, vol. 5, pp. 2874–2902, 2012.

[40] M. C. Ruiz-Cañas, L. M. Corredor, H. I. Quintero, E. Manrique, and A. R. R. Bohórquez, "Morphological and structural properties of amino-functionalized fumed nanosilica and its comparison with nanoparticles obtained by modified Stöber method," *Molecules*, vol. 25, no. 12, p. 2868, 2020.

[41] K. Xia, R. Z. Ferguson, M. Losier, N. Tchoukanova, R. Brüning, and Y. Djaoued, "Synthesis of hybrid silica materials with tunable pore structures and morphology and their application for heavy metal removal from drinking water," *Journal of Hazardous Materials*, vol. 183, no. 1-3, pp. 554–564, 2010.

[42] S. Wang, D. Yu, Y. Huang, and J. Guo, "The adsorption of sulphonated azo-dyes methyl orange and xylenol orange by coagulation on hollow chitosan microsphere," *Journal of Applied Polymer Science*, vol. 119, no. 4, pp. 2065–2071, 2011.

[43] Q. Wu, H. Liang, M. Li, B. T. Liu, and Z. K. Xu, "Hierarchically porous carbon membranes derived from PAN and their selective adsorption of organic dyes," *Chinese Journal of Polymer Science*, vol. 34, no. 1, pp. 23–33, 2016.

[44] K. Parida, K. G. Mishra, and S. K. Dash, "Adsorption of copper (II) on NH2-MCM-41 and its application for epoxidation of styrene," *Industrial and Engineering Chemistry Research*, vol. 51, no. 5, pp. 2235–2246, 2012.

[45] M. V. Subbaiah and D.-S. Kim, "Adsorption of methyl orange from aqueous solution by aminated pumpkin seed powder: kinetics, isotherms, and thermodynamic studies," *Ecotoxicology and Environmental Safety*, vol. 128, pp. 109–117, 2016.

[46] A. Mittal, A. Malviya, D. Kaur, J. Mittal, and L. Kurup, "Studies on the adsorption kinetics and isotherms for the removal and recovery of methyl orange from wastewaters using waste materials," *Journal of Hazardous Materials*, vol. 148, no. 1-2, pp. 229–240, 2007.

[47] M. A. Barakat, A. Q. Selim, M. Mobarak et al., "Experimental and theoretical studies of methyl orange uptake by Mn–rich synthetic mica: insights into manganese role in adsorption and selectivity," *Nanomaterials*, vol. 10, no. 8, p. 1464, 2020.

[48] A. Deb, M. Kanmani, A. Debnath, K. L. Bhowmik, and B. Saha, "Ultrasonic assisted enhanced adsorption of methyl orange dye onto polyaniline impregnated zinc oxide nanoparticles: kinetic, isotherm and optimization of process parameters," *Ultrasonics Sonochemistry*, vol. 54, pp. 290–301, 2019.

[49] Y. Yao, H. Bing, X. Feifei, and C. Xiaofeng, "Equilibrium and kinetic studies of methyl orange adsorption on multiwalled carbon nanotubes," *Chemical Engineering Journal*, vol. 170, no. 1, pp. 82–89, 2011.

[50] R. Huang, Q. Liu, J. Huo, and B. Yang, "Adsorption of methyl orange onto protonated cross-linked chitosan," *Arabian Journal of Chemistry*, vol. 10, no. 1, pp. 24–32, 2017.

[51] A. A. Jalil, S. Triwahyono, S. H. Adam et al., "Adsorption of methyl orange from aqueous solution onto calcined Lapindo volcanic mud," *Journal of Hazardous Materials*, vol. 181, no. 1-3, pp. 755–762, 2010.

[52] L. Zhou, C. Gao, and W. Xu, "Magnetic dendritic materials for highly efficient adsorption of dyes and drugs," *ACS Applied Materials & Interfaces*, vol. 2, no. 5, pp. 1483–1491, 2010.

[53] D. Zhang, H. E. Hegab, Y. Lvov, L. Dale Snow, and J. Palmer, "Immobilization of cellulase on a silica gel substrate modified using a 3-APTES self-assembled monolayer," *Springerplus*, vol. 5, no. 1, 2016.

[54] A. Farrukh, A. Akram, A. Ghaffar et al., "Design of polymer-brush-grafted magnetic nanoparticles for highly efficient water remediation," *ACS Applied Materials & Interfaces*, vol. 5, no. 9, pp. 3784–3793, 2013.